Magnetic resonance imaging of structure and convection in solidifying mushy layers

By PASCALE AUSSILLOUS[1], ANDREW J. SEDERMAN[2],
LYNN F. GLADDEN[2], HERBERT E. HUPPERT[1]
AND M. GRAE WORSTER[1]

[1]Institute of Theoretical Geophysics, Department of Applied Mathematics and Theoretical Physics,
University of Cambridge, Wilberforce Road, Cambridge CB3 0WA, UK

[2]Magnetic Resonance Research Center, Department of Chemical Engineering, University of Cambridge,
Madingley Road, Cambridge CB3 0HE, UK

We have used magnetic resonance imaging to study the structure of and convection within a solidifying mushy layer formed from an aqueous sucrose solution cooled from above. We focus on the situation in which dissolution channels, known as chimneys, are created by the action of buoyancy-driven convection. We have obtained high-resolution images of the microstructure formed by individual ice platelets and coarser-grained images that average over the platelets to show the geometry of the dissolution channels. We observe that the chimneys are branched and occur only in the lower part of the mushy layer. By acquiring low-resolution images rapidly, we have made detailed measurements of the thickness of the mushy layer, its porosity distribution and the number and total area of the chimneys. The mushy layer is seen to grow in a self-similar manner until internal convection begins, whereafter the solid fraction increases in the lower part of the layer.

1. Introduction

When a binary alloy is cooled below its liquidus temperature, one component solidifies preferentially, creating a porous matrix of solid crystals, with a complex small-scale geometry, bathed in a liquid phase more concentrated in the second component. This two-phase region comprising the solid matrix and the interstitial residual melt is called a mushy layer. For situations in which a binary alloy is cooled either from an upper or a lower horizontal boundary, Huppert & Worster (1985) showed that six different regimes of convection are possible depending on the relative buoyancy of interstitial melt and on the position of the cooling plate. In this study, we work with a system in which the density of the residual melt increases as the temperature decreases and its concentration correspondingly increases, and we cool it from the top. This configuration is both thermally and compositionally unstable, with the liquid inside the mushy layer being more dense than that below it. Convection can develop in the mushy layer, leading by dissolution to the formation of channels free of crystals, called chimneys, in which downflow occurs (Copley *et al.* 1970; Worster 2000).

Similar dynamic effects may occur in the Earth's core, within magma reservoirs and within sea ice. The situation we study here is similar to the drainage of brine through brine channels within sea ice (Wettlaufer, Worster & Huppert 1997). Similar effects occur during the casting of metallic alloys (Copley *et al.* 1970; Kurz & Fischer 1986).

Previous experimental studies, such as those by Huppert & Worster (1985), Chen & Chen (1991), Tait & Jaupart (1992), Bergman *et al.* (1997) and Wettlaufer *et al.* (1997) have tried to describe what is happening inside the mushy layer during solidification by indirect means, such as by studying the evolution of the bulk liquid properties (such as concentration or total volume) or by using local thermal probes to deduce the mean evolution of the mush. Observations have also been made of the interface between the liquid and the mushy layer to determine properties of the crystal matrix or the first appearance of chimneys (Tait, Jahrling & Jaupart 1992). Many measurements have been made *a posteriori*, once solidification has ceased. For example, measurements of local porosity, bulk composition and the dimensions of chimneys have been obtained by cutting the frozen mushy layer into slices (Turner & Gustafson 1981; Bergman *et al.* 1997; Turner, Huppert & Sparks 1986; Cottier, Eicken & Wadhams 1999). But this gives information only at the final instant. More sophisticated techniques have been used, such as X-ray tomography. With this technique, Chen (1995) obtained a short time sequence of the porosity evolution inside the mushy layer during solidification after the first appearance of chimneys and found structures similar to the C-profiles commonly measured in sea ice (e.g. Untersteiner 1968). Conductivity measurements have also been made to deduce porosities (Chiareli & Worster 1992; Notz, Wettlaufer & Worster 1997; Shirtcliffe, Huppert & Worster 1991). Here, we present a study of the evolution of the structure and porosity of the growing mushy layer as well as the chimneys during the solidification process using magnetic resonance imaging (MRI).

The MRI technique is being increasingly used in non-medical applications. MRI, in common with all magnetic resonance (MR) techniques, has five particular attributes advantageous to studying multi-component, multi-phase systems: it is non-invasive; optically opaque systems can be studied; different chemical species and phases can be identified and quantified; transport measurements can be made without the need for introduction of any tracer; and the direct use of the Fourier transform of the time-domain response of the whole system means that no model for image reconstruction is required.

MRI has been used previously to measure properties of sea ice (Callaghan *et al.* 1999; Eicken *et al.* 2000) and salt-water ice (Menzel *et al.* 2000) but most measurements were taken after solidification. Here we obtain direct, highly resolved observations and quantitative measurements of the evolution of structure and porosity inside the mushy layer during solidification.

This is the first experimental study of mushy layers to use sucrose solutions, which we chose (rather than salt water, for example) because it gives a good MRI signal owing to its high density of hydrogen nuclei and low dielectric constant, the latter enabling good tuning of the spectrometer receiver coil. We describe their physical properties in §2. The experimental apparatus is briefly described in §3, and the fundamentals of MRI as they relate to multi-phase systems are outlined in §4. MR images revealing the microstructure and channel geometry within the mushy layer are presented in §5. Some theoretical considerations in §6 aid the interpretation of our quantitative measurements, which are discussed in detail in §7. Our main conclusions are drawn in §8.

2. Properties of sucrose–water solutions

The equilibrium phase diagram of the sucrose–water solution is presented in figure 1. The curves of sucrose solubility and the liquidus, which intersect at the eutectic point ($T_E = -13.9\,^\circ\text{C}$), are shown in this figure as well as the curve of sucrose supersolubility. The liquidus curve defines the equilibrium between the saturated solution and ice.
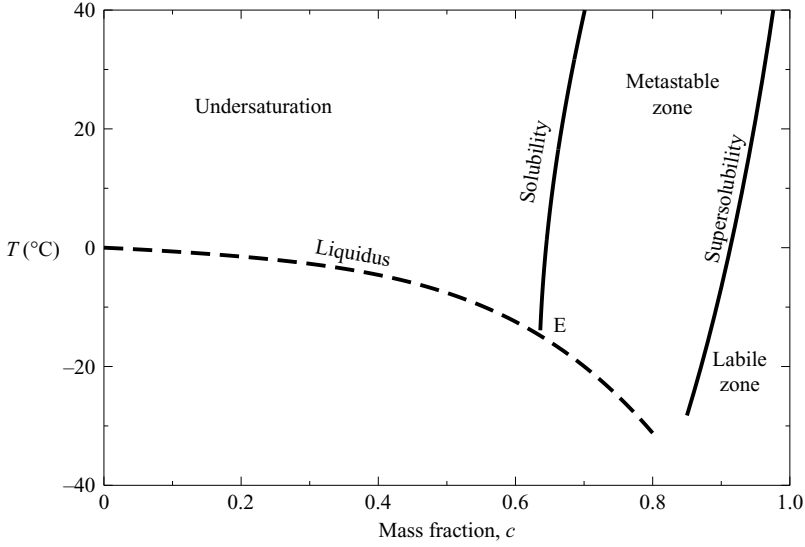
FIGURE 1. Phase diagram of the sucrose–water system showing the liquidus, solubility and supersolubility curves and the hypothetical eutectic point (E).

Below the eutectic temperature, ice continues to form whereas sucrose concentrates in a supersaturated solution. This thermodynamically unstable state is caused by the increase in viscosity and by limitation of movement of the molecules which worsen the conditions for formation of stable sugar-crystal nuclei. The eutectic point is then an extrapolated intersection between the sucrose solubility curve and liquidus curve and has no real experimental existence.

We have fitted data from Mathlouthi & Reiser (1995) to represent the liquidus curve by

$$T = T_\ell(c) \equiv -5.176\,c - 13.27\,c^2 + 24.16\,c^3 - 75.52\,c^4 \tag{2.1}$$

for $0 < c < 0.7$, where T_ℓ (°C) is the temperature of the freezing point of sucrose solution and c is the mass fraction of sucrose. The corresponding dependence between the concentration of sucrose c and the temperature T, for $-21\,°\text{C} < T < 0\,°\text{C}$, is fitted by

$$c = c_\ell(T) \equiv 3.2355 \times 10^{-3} - 1.6885 \times 10^{-1}T - 2.9460 \times 10^{-2}T^2 - 3.3994 \times 10^{-3}T^3$$
$$- 2.2722 \times 10^{-4}T^4 - 7.9522 \times 10^{-6}T^5 - 1.1224 \times 10^{-7}T^6. \tag{2.2}$$

The density of the solution increases monotonically with sucrose concentration and very slightly as the temperature decreases. We use the equation given by Ruddick & Shirtcliffe (1979), describing the solution density as a function of concentration and temperature, to obtain an approximation for the density at the liquidus concentration as a function of temperature alone (figure 2a). This plot can be fitted by the 6th-order polynomial

$$\rho_\ell = 1.0011 \times 10^{+3} - 6.82251 \times 10^{+1}T - 9.2800 \times T^2 - 8.7004 \times 10^{-1}T^3$$
$$- 4.7214 \times 10^{-2}T^4 - 1.3397 \times 10^{-3}T^5 - 1.53270 \times 10^{-5}T^6. \tag{2.3}$$

Sucrose–water solutions are well-represented as being Newtonian at all temperatures and concentrations. The viscosity of the sucrose–water solutions increases strongly with the sucrose concentration and as the temperature decreases. The model
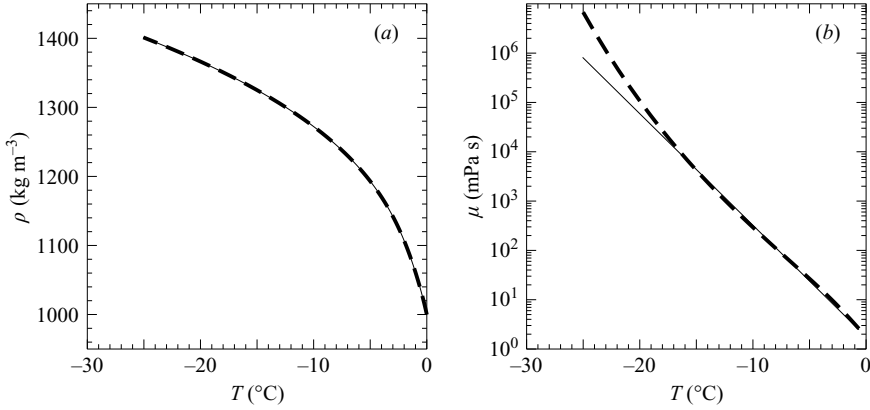
FIGURE 2. (*a*) Density against temperature at the liquidus concentration: the dashed line represents the equation given by Ruddick & Shirtcliffe (1979) extrapolated at the liquidus concentration and the full line represents equation (2.3). (*b*) Viscosity (on a logarithmic scale) against temperature at the liquidus concentration: the dashed line represents the model given in Mathlouthi & Reiser (1995) and the full line is (2.5).

given in Mathlouthi & Reiser (1995) is represented by

$$\log \mu = 22.46N - 0.114 + \psi(1.1 + 43.1N^{1.25}), \qquad (2.4)$$

where μ is the dynamic viscosity measured in mPa s, $N = 100c/(1900 - 1800c)$ is the mole fraction of sucrose, c is the concentration, $\psi = (30 - T)/(91 + T)$ and T is the temperature (°C). This equation is extrapolated to calculate the dynamic viscosity at the liquidus concentration as a function of temperature (figure 2*b*). This plot can be fitted approximately in the range $-17.5 < T < 0$ by an exponential function

$$\mu_\ell = \mu_0 e^{-T/T_\mu} = 1.77 e^{-T/1.92}, \qquad (2.5)$$

with a maximum error of 15 %.

The viscosity is high at low temperature and high concentrations. For example, it is approximately 10 000 times the viscosity of water at -17.5 °C at the liquidus concentration. This inhibits the onset of convection, which allows a longer period in which to study the evolution of the mushy layer prior to the formation of chimneys compared with experiments in which ammonium–chloride solutions are used (Chen & Chen 1991).

We consider the solid density to be constant and given by $\rho_s = 916.2$ kg m^{-3}. We also consider the following quantities to be independent of the temperature and phase: the specific heat capacity $c_p \approx 3$ kJ kg^{-1}, the latent heat $L \approx 334$ kJ kg^{-1} and the thermal diffusivity $\kappa \approx 1.4 \times 10^{-7}$ m^2 s^{-1}. These values are taken to represent both solid- and liquid-phase properties.

3. The experimental apparatus

The experimental apparatus consisted of a long cylindrical Perspex tube and a surrounding glass jacket that fitted snugly in the 6 cm diameter core of the magnet of an MR instrument. The working section of the tube had an internal diameter of 3.7 cm and depth of 18 cm, and was filled with a solution of sugar and water (figure 3). The cylindrical glass jacket had an internal circulation of a water–ethylene-glycol solution at -3 °C to insulate the experimental section from ambient temperatures. The tank
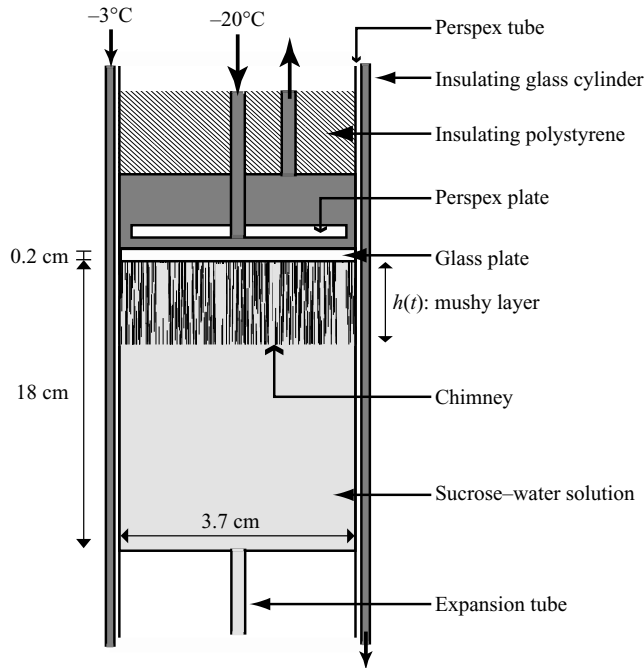
FIGURE 3. Sketch of the experimental set-up placed within the core of the MRI apparatus.

c_0	0.1	0.2	0.2	0.2	0.3	0.3	c_0	0.1	0.1	0.2	0.2	0.3	0.4
T_b (°C)	−5	−20	−5	−3	−10	−7	T_b (°C)	−20	−20	−20	−20	−20	−20

TABLE 1. Laboratory experiments performed in the cubic (left) and the cylindrical (right) tank.

was cooled from the top via a 2 mm thick glass plate in contact with a circulating water–ethylene-glycol mixture at −20 °C, which is well below the liquidus temperature. We used a glass plate instead of a metal plate (which would provide more efficient heat transfer) because metal generates strong signal disturbances in MRI. However, the thermal conductivity of glass (approximately $1 \, \text{W m}^{-1} \, \text{K}^{-1}$) is sufficiently high to allow horizontally homogenous cooling.

Complementary experiments were performed in the laboratory using the same apparatus as in the MRI experiment, but held in ambient air (around 20 °C), as well as a more standard apparatus consisting of a cubic tank with sides of 20 cm. This tank was made of Perspex with a brass cooling plate through which thermally regulated ethylene glycol was circulated. This set-up allowed us to investigate a bigger volume with better thermal insulation (performed with thick polystyrene blocks). We monitored the time evolution of the mush–liquid interface as well as the temperature at different positions in the tank (0, 0.6, 2.7, 5.7, 8.8, 11.9, 14.8 and 16.8 cm from the cooling plate).

We performed six experiments in each geometry, as reported in table 1, with different initial concentrations c_0 and top temperatures T_b.

4. Magnetic resonance imaging

The general principles of MRI are briefly described in the following three paragraphs. The remainder of this section gives specific details of the MRI set-up we used.

An understanding of the experimental results (§ 5 onwards) does not rely on these details.

Two different types of MR data are presented. First, MR microimaging is used to identify the phase evolution of the system and discriminate bulk solution, mushy layer, crystal structure and the location of chimneys. From these data the porosity distribution within the mushy layer is obtained. Secondly, the velocity of the liquid within chimneys is measured using MR velocity imaging methods. For an introduction to the principles of MR techniques, the reader is referred to excellent texts by Callaghan (1991) and Kimmich (1997). There are also reviews of the application of MR techniques to studies of fluid mechanics (Fukushima 1999), the development of fast imaging sequences to study non-medical systems (Mantle & Sederman 2003), and the use of combined MR spectroscopy, diffusion and imaging methods to study physical and chemical processes over multiple length scales (Gladden, Mantle & Sederman 2004).

The physical principle upon which MR measurement is based is that when a nucleus of non-zero spin is placed in a magnetic field B_0 (typically a superconducting magnetic field of 2–10 T), its nuclear-spin angular momentum energy levels are made non-degenerate and the spin axis is caused to precess. By exposing the system to electromagnetic energy in the radio-frequency (r.f.) range, a resonant absorption occurs between these nuclear-spin energy levels. The resonant precessional frequency ω_0 is proportional to the strength of the magnetic field B_0 used in the experiment,

$$\omega_0 = \gamma B_0, \tag{4.1}$$

where γ is the gyromagnetic ratio, which is an isotope-specific property. The return of the spin system to equilibrium is monitored as a decaying induced voltage detected by a receiver coil placed around the sample. To perform an MRI experiment, a spatially varying magnetic field is imposed on the sample in addition to the large static field B_0 so that the resonance frequency of species within the sample becomes a function of position and the data can thereby be spatially resolved. The measurement is calibrated such that the relationship between resonance frequency and spatial position is known.

In this study we have a complex multi-phase system in which the same chemical species may be present in one or more phases. Discrimination between phases and quantification of porosity are achieved by exploiting the contrast of nuclear-spin relaxation times between phases. Following the application of the r.f. excitation pulse, the nuclear-spin system has excess energy. The return to thermal equilibrium is characterized by two relaxation times: the spin–lattice relaxation time T_1; and the spin–spin relaxation time T_2. The former characterizes the energy exchange between the excited spin and the surrounding physical environment (i.e. the lattice), while the latter characterizes the loss of phase coherence within the spin system itself. Both are influenced by the physico-chemical environment of the molecules being studied. In all the systems we studied, T_1 was less than 1 s, ranging from about 900 ms for a 10 wt % (mass fraction 0.1) sucrose solution to about 220 ms for a 69.6 wt % solution. In all image acquisitions, recycle times were 3 s, and therefore signal contrast arising from T_1 effects is negligible. Contrast in our images is therefore based entirely on T_2.

All imaging experiments were performed on a Bruker Spectrospin DMX 200, 4.7 T vertical-bore magnet using a birdcage r.f. coil of length and internal diameter 6.4 cm. [1]H images were acquired at a frequency of 199.7 MHz. Spatial resolution was achieved using shielded gradient coils providing a maximum gradient strength of 13.50 G cm^{-1}. The T_1 characteristics of the system were measured using inversion recovery methods and the T_2 characteristics were measured using CPMG and Hahn-echo methods
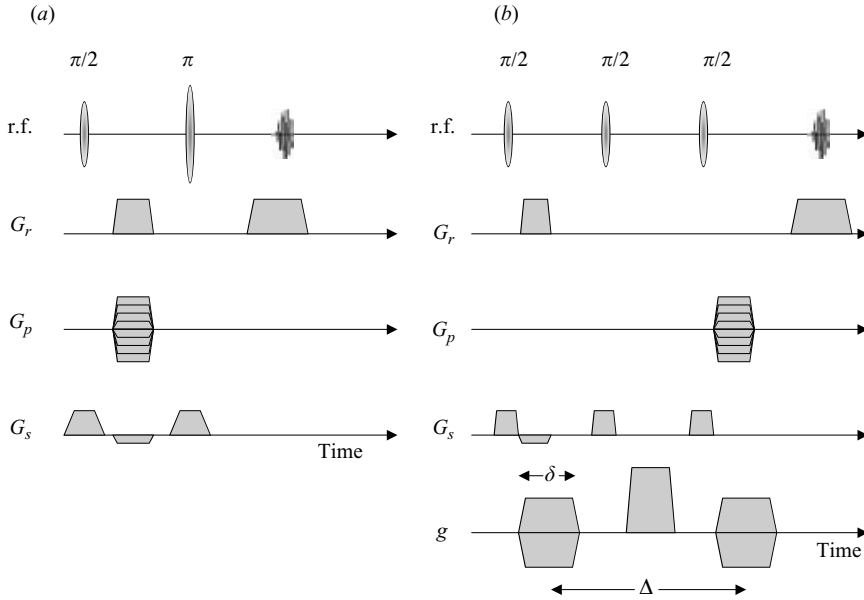
FIGURE 4. (*a*) Schematic of the pulse sequence used for the micro-imaging studies. In this spin-echo sequence both pulses are slice selective so that multiple slices can be acquired without increasing the image acquisition time. (*b*) Schematic of pulse sequence used for velocity images. Again slice-selective pulses are used throughout so that multi-slice techniques can be used. Two values of the velocity gradient *g* were used and a homospoil gradient was applied between the 2nd and 3rd r.f. pulses.

(Callaghan 1991). Images were acquired using a standard multi-slice spin-echo pulse sequence (figure 4). This enables several parallel images to be acquired in the time normally taken to acquire a single image. The $\pi/2$ r.f. excitation pulse and π refocusing pulse were both Gaussian-shaped selective r.f. pulses, 512 μs in duration and an acquisition width of 200 kHz was used.

In the microimaging studies (figure 6 for example) discrimination between bulk solution, mushy layer and chimneys is achieved because of the very short T_2 value ($\sim 15\,\mu$s) characterizing the solid phase. Since an echo time of 2.5 ms is used in all imaging experiments, negligible signal intensity is obtained from the solid. Thus, signal is only acquired from the liquid phase, and the signal intensity within the mushy layer is proportional to the fraction of solid present within any given image pixel.

The signal intensity is additionally sensitive to the sucrose concentration in the residual liquid, owing predominantly to the decrease in molecular mobility of sucrose, which reduces the T_2 values characterizing the system. Independent measurements of signal attenuation were made on sucrose solutions of known concentrations held at their liquidus temperature for 15 minutes before the measurements were taken. The spin-echo time in these calibration experiments was the same as in the experiments to measure porosity. The calibration experiments enable us to determine a multiplicative correction to apply in our quantitative evaluations of porosity (figure 5). Note that the multiplicative correction is close to 1 and led to less than 10 % error for temperatures above $-13\,^{\circ}$C. It can be represented by the polynomial

$$C_{cor} = 9.9951 \times 10^{-1} + 1.6172 \times 10^{-2}T + 7.6525 \times 10^{-3}T^2$$
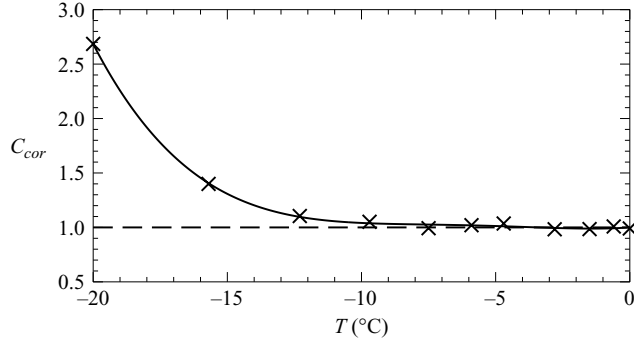$$+ 9.9256 \times 10^{-4}T^3 + 4.3047 \times 10^{-5}T^4, \tag{4.2}$$

FIGURE 5. Multiplicative correction applied to the low-resolution data to obtain the quantitative porosity. The curve corresponds to the polynomial fit given in (4.2).

	High resolution	Medium resolution	Low resolution
In-plane resolution	98 μm × 98 μm	190 μm × 190 μm	780 μm × 780 μm
Slice thickness	0.5 mm	1 mm	2 mm
Inter-slice separation	4 mm	2 mm	4 mm
Data array xy	512 × 512	256 × 256	64 × 64
Data array zx	1024 × 512	512 × 256	128 × 64
Acquisition time	43 min	13 min	3.2 min

TABLE 2. Parameters of the magnetic resonance images.

so that the liquid fraction is given by

$$\chi = C_{cor} I / I_0, \tag{4.3}$$

where I is the measured signal intensity and I_0 is the intensity measured in the fully liquid region.

Images were acquired for transverse (i.e. horizontal) and vertical sections through the sample at three different spatial resolutions: high-resolution images were used to capture details of the crystal structure within the mushy layer; medium-resolution images showed the structure of the dissolution channels (chimneys); and rapid, low-resolution images were used to measure the temporal evolution of the local mean solid fraction distribution. Details are shown in table 2.

The principles of MR transport measurements are discussed in detail by Fukushima (1999). A number of approaches exist but the most robust and quantitative are those based on 'phase-shift' (or 'pulsed gradient') methods. In summary, the application of a pulsed magnetic field gradient at the beginning of an experiment encodes a given spin with a 'label' describing its position along the direction of the applied gradient. At a time Δ later, referred to as the observation time, a second pulsed gradient is applied. The net effect of applying these two gradients is to introduce a phase shift in the orientation of the nuclear spin system which is directly related to the distance travelled in the direction of the applied gradients. By careful selection of the magnitude of the applied field gradients and the observation time used between the two pulsed gradients, velocities from approximately 10^{-1} to $1\,\mathrm{m\,s^{-1}}$ can be measured.

In our velocity imaging experiments the echo time T_E was 10.3 ms, while the observation time Δ was 200 ms . Two values of the pulsed magnetic field gradient g were used, of opposite polarities: -6.5 and $+5.5\,\mathrm{G\,cm^{-1}}$, both with a duration δ
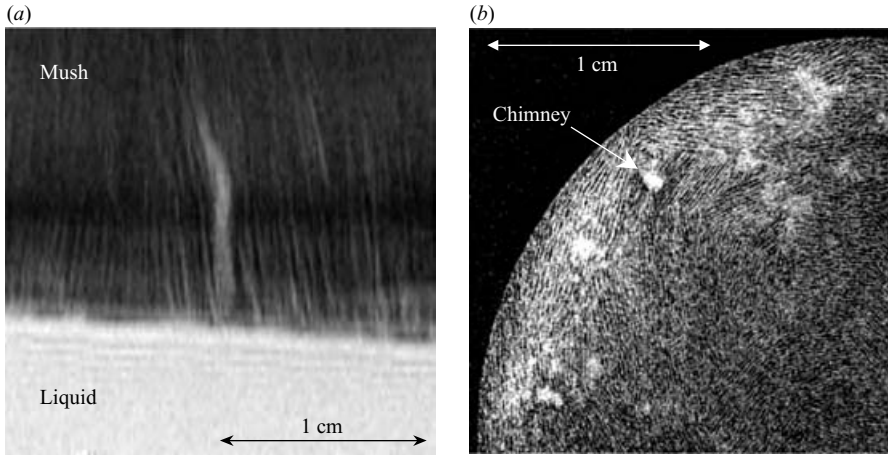
FIGURE 6. Platelet structure of the ice in the mushy layer, viewed from (*a*) vertical and (*b*) horizontal slices obtained using the highest resolution (98 μm × 98 μm) for a solution with an initial concentration $c_0 = 0.2$.

of 2 ms. Opposite polarities of similar magnitude were selected to minimize diffusive attenuation (proportional to the square of the gradient) while maximizing the phase shift between the two velocity-encoded images. The recycle time was 4 s and the signal was averaged over two scans, giving a total data acquisition time of 68 min. The field of view is 50 mm × 50 mm, recorded as a 256 × 256 pixel array, thereby yielding an in-plane spatial resolution of 195 μm × 195 μm. The slice thickness was 2 mm.

The contributions of magnetic susceptibility to T_2 were found to be negligible.

5. Structural observations

As we cooled the sample below the liquidus temperature, a mushy layer developed with a solid phase made of pure ice. The liquid phase corresponded to a mixture of sucrose and water more concentrated in sucrose than initially. Because we cooled the tank from the top and the liquid density increases with sugar concentration, the system became unstable and began to convect, which led to the formation of chimneys. The MRI allowed us to follow directly what was happening locally inside the mushy layer during solidification.

Once the mushy layer had grown for several hours and its evolution had slowed, we could distinguish the ice structure using the highest resolution (98 μm × 98 μm), as can be seen in figure 6, which shows a vertical and a horizontal slice in an experiment with an initial concentration $c_0 = 0.2$. Figure 6(*b*) shows a brighter region (more liquid) around the edges of the sample and more chimneys there. This image was taken before the addition of the cooling jacket. Later experiments, using the cooling jacket, were more uniform horizontally both in mean intensity and in number density of chimneys (see figure 7, for example). In the vertical slice, the mushy layer is the dark striated region and the pure liquid is the light, homogeneous region below. The horizontal slice is taken just above the mush–liquid interface. It can be readily distinguished in both images that the ice forms approximately vertical platelets with a typical width of about 200 μm. Some liquid-filled channels (chimneys), a millimetre or so across, can also be seen in the horizontal slice. Note that the geometry of the
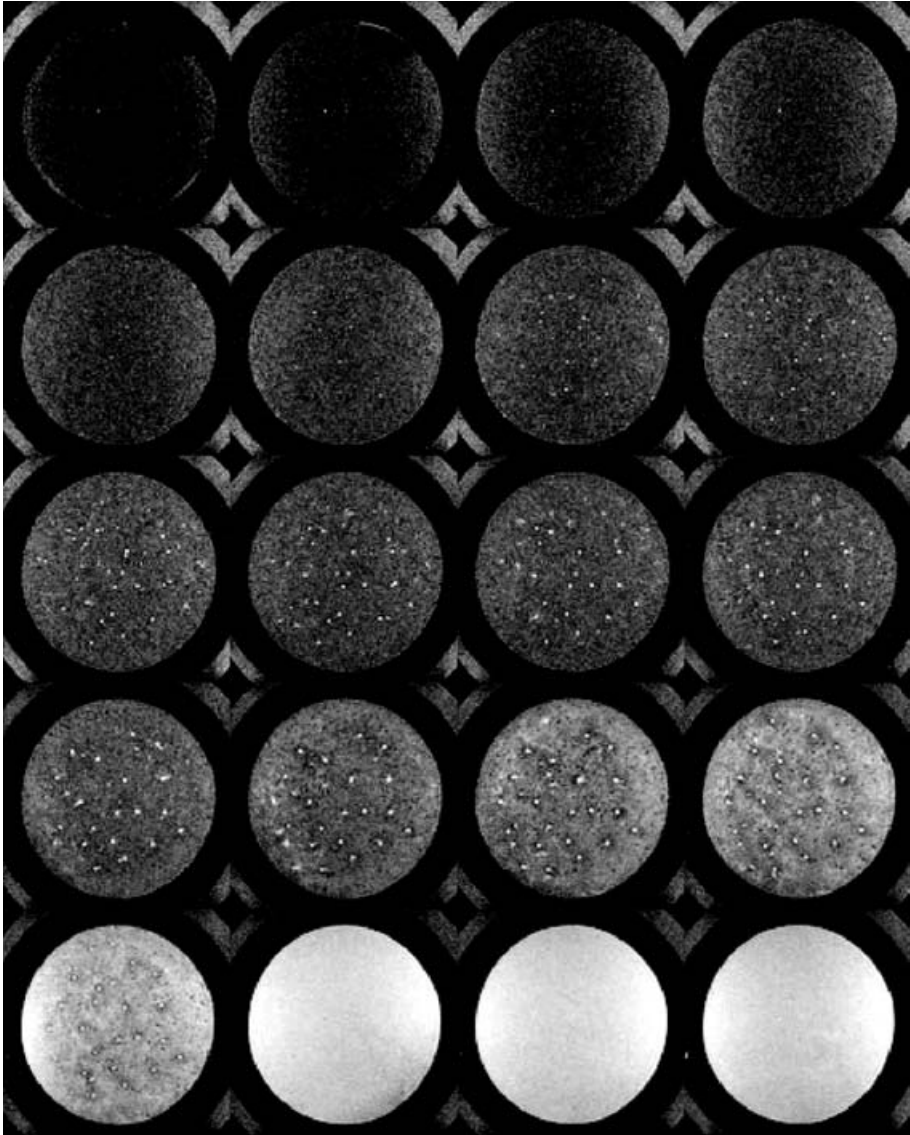
FIGURE 7. Sequence of horizontal slices (resolution $190\,\mu m \times 190\,\mu m$) for a solution with an initial concentration $c_0 = 0.2$ after about 2.8 hours of solidification for different position into the sample. The scale is given by the cylinder diameter which is 3.7 cm. The distances from the cooling plate, from left to right and top to bottom, range from 1 mm to 39 mm, 2 mm apart.

channels seems largely unaffected by the platelet structure of the ice crystals, which was also noted by Wettlaufer *et al.* (1997) in the context of sea ice.

Using the medium resolution ($190\,\mu m \times 190\,\mu m$), we obtained precise images of the chimneys, when they occur, in vertical and horizontal slices. Figure 7, corresponding to a solution with an initial concentration $c_0 = 0.2$ after about 2.8 hours of solidification, shows the typical images obtained in horizontal slices, 2 m apart, from the top (inside the mushy layer) to the bottom (inside the liquid).

The first slice is in the mush, 1 mm away from the cooling plate. The image is quite dark which shows that the mush has quite a small porosity. Then, as we move
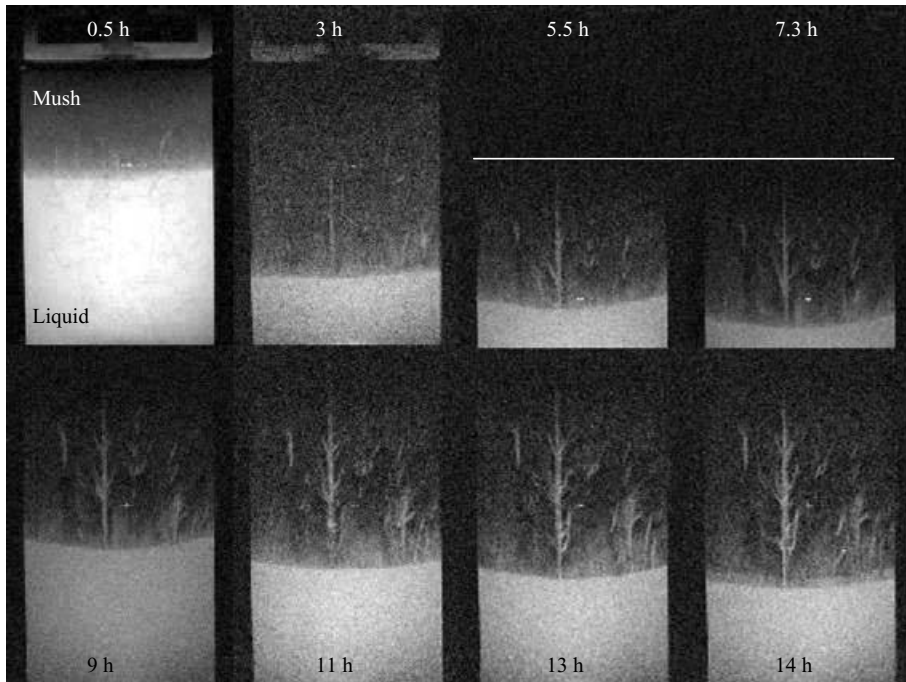
FIGURE 8. Time sequence of a vertical slice (resolution $190\,\mu m \times 190\,\mu m$) located in the centre of the cylinder for a solution with an initial concentration $c_0 = 0.2$. Above the white line, there is no information because the whole sample was translated upwards. The scale is given by the cylinder diameter which is 3.7 cm.

through the sample towards the liquid, the images become lighter, which shows that the mush is more porous. The slices at 35, 37 and 39 mm away from the cooling plate are in the liquid (which appears bright in the MRI images).

The chimneys can be easily identified: they appear as bright disks because they are full of liquid. In contrast with previous observations (Chen & Chen 1991; Chen 1995), in different systems, the chimneys do not span the full depth of the mushy layer. Indeed, they are visible only from 17 mm away from the cooling plate. Moreover, they seem to have a larger diameter close to the mush–liquid interface.

In figure 8, a time sequence of the evolution of a central vertical slice is shown for a solution with an initial concentration $c_0 = 0.2$. During the first half hour, the mushy layer grows without any chimneys. Then, after about 3 hours, chimneys can be readily distinguished, growing with the mushy layer. This delay can be explained in terms of the increasing Rayleigh number associated with the mushy layer as it thickens (Wettlaufer *et al.* 1997). An interesting feature is that the chimneys appear to be highly branched. This behaviour was also found by Tait & Jaupart (1992), who observed that at low solution viscosities the chimneys penetrate the whole mush and have a roughly constant diameter whereas at higher solution viscosities they do not always penetrate the whole mush but broaden out into a 'root' structure.

The MRI thus provides interesting observations of the different scale of structures within the mushy layer. Furthermore, quantitative information of the local porosity distribution within the mushy layer can be obtained. Using the low-resolution data ($780\,\mu m \times 780\,\mu m$ per pixel), we obtained the horizontally averaged porosity as a function of vertical position. In order to obtain accurate porosity values from the

c_0	t (h:min)
0.1	0:00, 0:09, 0:18, 0:27, 0:36, 0:46, 0:55, 1:04, 1:12, 1:21, 1:30, 1:39, 1:47, 2:14, 2:22, 2:49, 2:58, 3:24, 3:33, 3:59, 5:16, 5:43, 6:52, 7:46, 9:50, 10:00, 11:19, 12:13, 13:32, 14:26, 15:42, 16:37, 17:56
0.2	0:10, 0:22, 0:30, 1:25, 1:57, 2:05, 2:29, 2:38, 3:02, 3:11, 3:44, 4:11 5:22, 6:01, 7:11, 7:50, 9:01, 9:40, 10:51, 11:30, 12:40, 13:19, 14:30, 15:08
0.3	0:09, 0:18, 0:28, 0:37, 0:46, 0:55, 1:04, 1:12, 1:22, 1:30, 1:57, 2:05, 2:32, 2:40, 3:07
0.4	0:09, 0:18, 0:27, 0:36, 0:45, 0:54, 1:04, 1:12, 1:35, 1:43, 2:05, 2:25, 2:53, 3:03, 3:19, 4:10

TABLE 3. Times in hours and minutes at which porosity measurements were made by MRI for four experiments with different initial concentrations c_0.
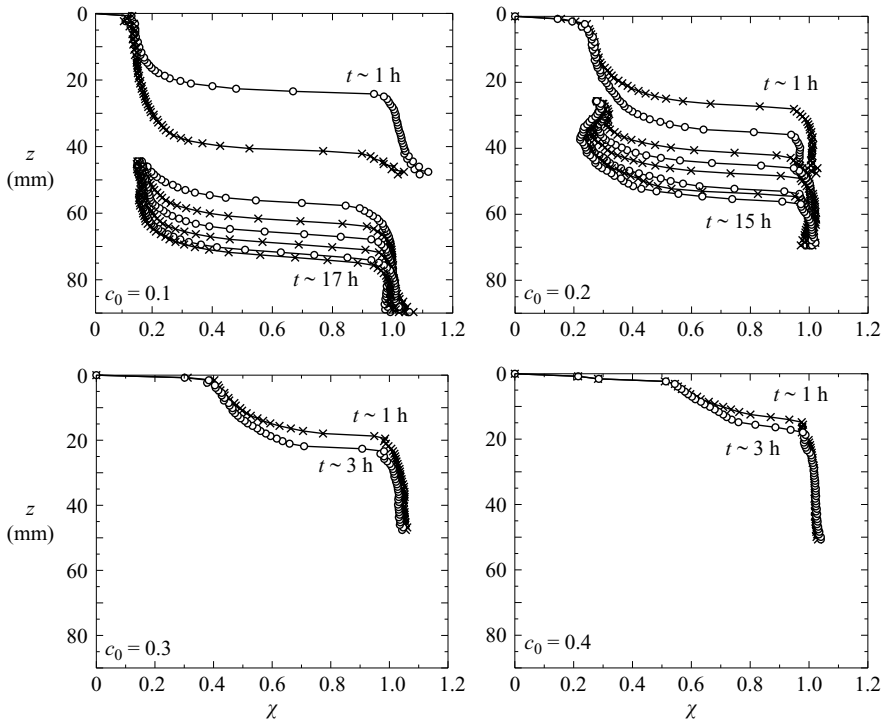

FIGURE 9. Mean porosity χ, averaged horizontally, as a function of vertical position z from the bottom of the cooling plate at different times and for the four initial sucrose concentrations $c_0 = 0.1, 0.2, 0.3$ and 0.4. There are differences of two hours between successive curves and the 5 h curve is missing from the $c_0 = 0.1$ solution.

MRI data, account had to be taken of the local interstitial sucrose concentration. This was deduced by assuming that the interstitial liquid was in local thermodynamic equilibrium and that the temperature field in the mushy layer was linear, and by using the correction factor displayed in figure 5. The different times at which the porosity data were taken are show in table 3.

In figure 9, we present the horizontally averaged porosity as a function of the vertical position inside the mushy layer for different times and the four initial sucrose
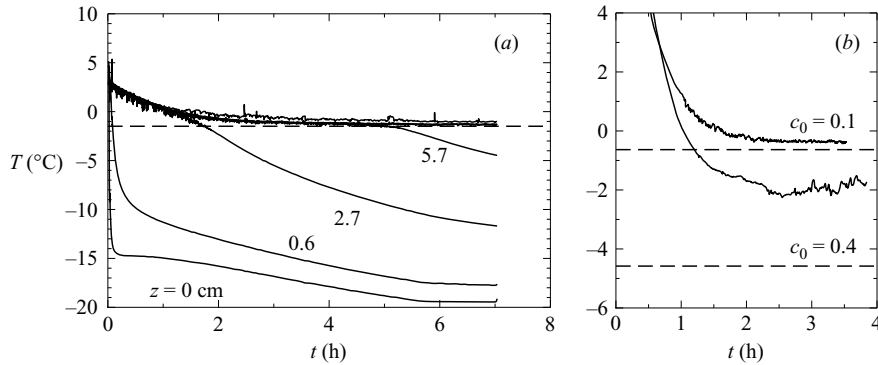
FIGURE 10. Temperature at different positions in the cooled tank. (*a*) $c_0 = 0.2$ aqueous sucrose solution in a cubic tank, with the cooling plate at $T_b = -20\,^\circ$C. The different curves correspond to different positions in the tank from bottom to top (0, 0.6, 2.7, 5.7, 8.8, 11.9, 14.8 and 16.8 cm from the cooling plate). (*b*) Cylindrical tank, liquid temperature for $c_0 = 0.1$ and $c_0 = 0.4$, cooled at $-20\,^\circ$C with the cooling jacket at $-3\,^\circ$C. The dashed lines represent the respective liquidus temperatures.

concentrations $c_0 = 0.1, 0.2, 0.3$ and 0.4. There is 2 hours difference between successive curves. These curves are qualitatively similar to those found in previous studies (Shirtcliffe *et al.* 1991; Chen 1995). Notice that the growth rate of the mushy layer slows down with time. Also, there is faster growth in the solutions that were initially less concentrated, and these form mushy layers of lower porosity.

6. Theoretical considerations

Some essential theoretical ideas assist with the interpretation and analysis of our data. We represent the mushy layer as a continuum, with local mean volume fraction of solid ϕ and porosity $\chi = 1 - \phi$. We denote the mass concentration of sucrose in the interstitial liquid by c and the temperature by T. The governing equations inside the mushy layer are given by local conservation of heat, mass and solute and Darcy's equation for flow through porous media (Tait & Jaupart 1992; Chiareli & Worster 1992; Worster 2000).

The growth of the mushy layer is determined principally by thermal balances (Huppert & Worster 1985) and, in principle, the thermal field can be determined by solving the heat conservation equation augmented by a source term related to the internal release of latent heat (Worster 2000). However, in our modelling here, we use the simple approximation of a linear temperature profile, guided by our laboratory experiments, as follows.

Because of the constraints on space within the magnet and the need to avoid using metallic components within the sample, no temperature measurements were made during the MRI experiments. We therefore conducted separate, similar experiments in the laboratory, where detailed measurements and visual observation could be made. In figure 10(*a*), we see a typical temperature record in the cubic tank with thermistors placed at different vertical positions during an experiment with a water–sucrose solution of initial concentration $c_0 = 0.2$, cooled at the top at $T_b = -20\,^\circ$C. The liquid cools to the liquidus temperature within about two hours.

In figure 10(*b*), a record of the liquid temperature inside the cylindrical apparatus used in the MRI is shown as a function of time for the two extreme sucrose

concentrations ($c_0 = 0.1$ and $c_0 = 0.4$) maintained at the top at $-20\,°C$ and with the cooling jacket set at $-3\,°C$. The liquidus temperature in each case is depicted by the dashed line and it can be seen that the liquid temperature is above the liquidus temperature, which implies that the heat gain in this system is significant even with the surrounding cooling jacket. This effect is stronger for higher concentration (more than $2\,°C$ for $c_0 = 0.4$) as the cooling jacket temperature is then above the liquidus temperature.

Measurement of the temperature just below the glass plate gave a final temperature $T \approx -16\,°C$, reached about $180\,min$ after the commencement of the ethylene glycol circulation. We can then suppose that the experimental cooling temperature T_b was between $-16\,°C$ and $-20\,°C$.

Based on these observations and noting that the Rayleigh number within the liquid region was about 10^6, well above the critical value for convective instability to develop, we suppose that the liquid region is well mixed, of constant and uniform temperature equal to the liquidus temperature $T_\ell(c_0)$ at the initial concentration c_0 (Kerr *et al.* 1989). Moreover, given that the Stefan number $S = L/(c_p \Delta T)$, where $\Delta T = T_\ell(c_0) - T_b$, is large (about 7) in our experiments, we assume a linear temperature field in the mush so that

$$T = T_b + [T_\ell(c_0) - T_b]\frac{z}{h(t)}, \tag{6.1}$$

where $h(t)$ is the thickness of the mushy layer.

Solute conservation is given by

$$\rho_l(1 - \phi)\frac{\partial c}{\partial t} + \rho_l \boldsymbol{u} \cdot \nabla c = \rho_s c \frac{\partial \phi}{\partial t}, \tag{6.2}$$

if we suppose that chemical diffusion can be neglected compared with thermal diffusion, and we suppose that the mush is in local thermodynamic equilibrium, so the concentration and temperature fields are linked by the liquidus relationship

$$c = c_\ell(T). \tag{6.3}$$

The local mean density is given by $\overline{\rho} = \phi \rho_s + (1 - \phi)\rho_l$, where the subscripts s and l denote solid and liquid respectively. Conservation of mass is then given by

$$\frac{\partial \overline{\rho}}{\partial t} + \nabla \cdot (\rho_l \boldsymbol{u}) = 0, \tag{6.4}$$

where $\boldsymbol{u}$ is the volume flux of interstitial liquid per unit of area of mushy layer. We considered the variation of the density with the physical state because Chiareli & Worster (1992) have shown that neglect of this can lead to an error of $10\,\%$ in the prediction of the solid fraction. However, we use the Boussinesq approximation and consider $\rho_l = \rho_l[c_0, T_L(c_0)]$ to be independent of temperature and concentration.

In the absence of buoyancy-driven convection in the mushy layer, equations (6.2) and (6.4) can be solved for the velocity and the solid-fraction distribution subject to boundary conditions of zero velocity at the cooling plate and zero solid fraction at the mush–liquid interface.

The thickness of the mushy layer $h(t)$ is in principle determined by conservation of heat at the mush–liquid interface, expressed by

$$\rho_s L \dot{h} \phi = k_m \nabla T|_m - F_T, \tag{6.5}$$

where k_m is the mean thermal conductivity of the mushy layer, F_T is the heat flux from the liquid region and the dot denotes differentiation with respect to time. However,

in this study we do not have a means to determine F_T and so simply determine the various fields in terms of $h(t)$.

Buoyancy-driven flow in the mushy layer, when it occurs, is governed by Darcy's equation

$$\frac{\mu}{\Pi} \boldsymbol{v} = -\nabla p + \Delta \rho \boldsymbol{g}, \tag{6.6}$$

where p is the dynamical liquid pressure, $\Delta \rho = \rho(c, T) - \rho(c_0, T_\ell(c_0))$ and Π is the permeability of the mushy layer. Scaling of the governing equations (Worster 2000) reveals that convection in the mushy layer is dictated by a porous-medium Rayleigh number

$$Ra = \frac{\Delta \rho g \overline{\Pi} h}{\overline{\mu} \kappa}, \tag{6.7}$$

where $\overline{\mu}$ and $\overline{\Pi}$ are the mean viscosity and permeability of the layer. This Rayleigh number has been used successfully to correlate data relating to the onset of convection in sea ice (for example) by Wettlaufer *et al.* (1997). The Rayleigh number increases during our experiments as h increases, and can exceed the critical threshold for the onset of convection.

When there is no convection in the mushy layer, its structure depends only on the vertical position from the cooling plate z. It was shown by Huppert & Worster (1985) that the mushy layer then evolves in a self-similar fashion with similarity variable

$$\xi = z/h(t), \tag{6.8}$$

while the mushy-layer thickness increases proportionally to the square root of time,

$$h = 2\lambda \sqrt{\kappa t}, \tag{6.9}$$

where λ is a parameter that depends on the initial concentration of the solution and the boundary temperatures (Worster 2000).

Using this similarity variable, considering the linear temperature profile and scaling the vertical velocity $w = \sqrt{(\kappa/t)} f(\mu)$, we obtain the non-dimensional governing equations

$$\phi' = \frac{c'}{rc} \left(1 - \phi - \frac{f}{\lambda \xi} \right), \qquad f' = \xi \lambda (r - 1) \phi', \tag{6.10}$$

where $r = \rho_s/\rho_l$, primes denote differentiation with respect to ξ,

$$c = c_\ell(T) \quad \text{and} \quad T = T_b + \Delta T \xi. \tag{6.11}$$

The boundary conditions are that $f = 0$ at the cooled boundary $\xi = 0$ and $\phi = 0$ at the mush–liquid interface $\xi = 1$.

However, if we consider that the transport of solute into the mush due to the ice expansion is small ($\boldsymbol{u} \cdot \nabla C$ is negligible), then equation (6.2) can be integrated directly to give the porosity as a function of the local concentration

$$\phi = 1 - \left(\frac{c_0}{c} \right)^{1/r} \tag{6.12}$$

(Flemings & Nereo 1967), where $c = c(\xi)$ is determined from (6.11).

Equations (6.10) were solved numerically for ϕ and f using a shooting method, and the results compared with equation (6.12). With our parameters ($T_b = -17\,°C$ and c_0 varying from 0.1 to 0.4) the relative error in the porosity is everywhere less than about 8 %, decreasing away from the plate and with increasing initial concentration.
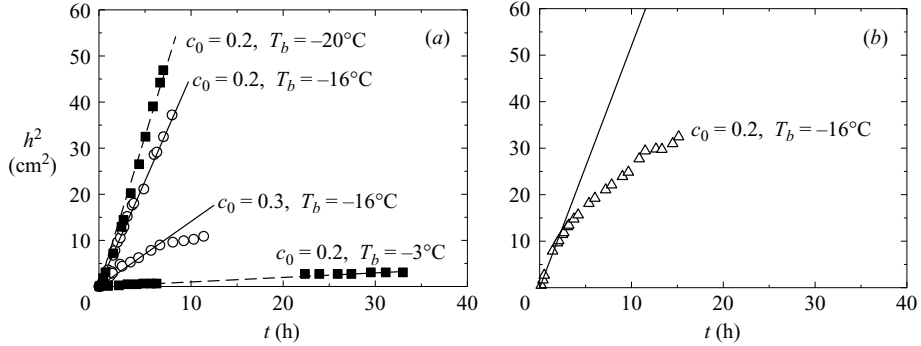
FIGURE 11. Square of the thickness of the mushy layer as a function of time for (*a*) the laboratory and (*b*) the MRI experiments. The laboratory cubic tank is represented by full squares and the cylindrical tank by circles, with triangles for the MRI experimental study. The concentration and the top-plate temperature are indicated. The line (dashed for the cube and full for the cylinder) represent the best fit given by (6.9).

The absolute error in porosity is no more than 0.023 in all cases. We therefore use the analytical result (6.12) to discuss our experimental results.

7. Quantitative results

7.1. *Thickness of the mushy layer*

The time variation of the thickness of the mushy layer was measured during laboratory experiments using the cubic and cylindrical tanks as well as during the MRI experiment. In the cubic tank the thickness was measured directly. In the MRI experiments, we used the porosity data, which can be seen for example in figure 9. The transition zone corresponding to the interface is diffuse and so to determine the position of the interface we use the porosity data above this zone and extrapolate them to obtain the intersection with the porosity $\chi = 1$ corresponding to the liquid. This is a valid process given that the porosity tends smoothly to 1 as the mush–liquid interface is approached (Worster 1986, 2000).

The results obtained are shown in figure 11, where the square of the mushy layer thickness is presented as a function of time for the laboratory and MRI experiments. It can be seen on this graph that at early times all the experiments are described well by (6.9), with a coefficient λ dependent on the conditions of the experiment. It can also be seen that after some time, for some experiments in the cylindrical tank, the thickness variation departs from this trend to follow a slower growth. The time at which the deviation occurs seems not to be reproducible. For example, in figure 11 it can be seen that in the laboratory experiment there is no visible deviation after 8 hours whereas for the same experimental conditions ($c_0 = 0.2$ and $T_b \approx -16\,°C$) in the MRI we observe a deviation after 2 hours of cooling. The times of deviation for $c_0 = 0.1, 0.2, 0.3$ and $c_0 = 0.4$ are about 3, 2, 1 and 1 hours after the beginning of solidification respectively. We believe that this effect is due to heat exchange with the surroundings rather than to internal dynamics such as the onset of convection.

7.2. *Solid-fraction distribution*

Before the onset of convection and the appearance of chimneys inside the mushy layer, we expect the porosity to follow a self-similar variation given by (6.11) and
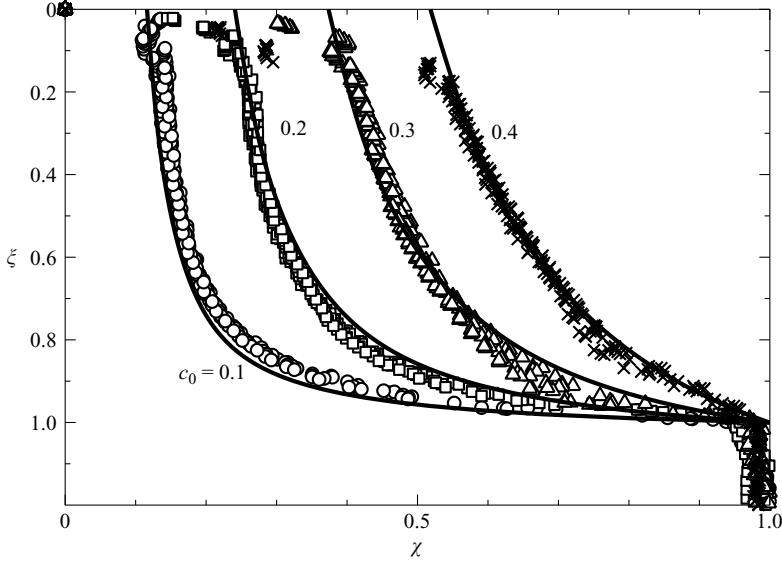
FIGURE 12. Similarity solutions of the porosity χ as a function of $\xi = z/h(t)$ for the four different concentrations at early times: $c_0 = 0.1$ and $0.75 < t < 1.8$ h (8 sets of data, circles); $c_0 = 0.2$ and $1.4 < t < 3.2$ h (7 sets of data, squares); $c_0 = 0.3$ and $0.8 < t < 2.7$ h (10 sets of data, triangles); and $c_0 = 0.4$ and $0.7 < t < 3.7$ h (12 sets of data, crosses). The prediction of the model given by (6.12) with $T_b = -17\,^\circ$C is plotted as a continuous curve for each initial concentration.

(6.12). Note that this result relies only on the concentration field varying according to the liquidus between $c_\ell(T_b)$ and c_0, and so does not depend on the temperature of the melt region nor on the variation of $h(t)$. To check this hypothesis, we plot the similarity variable ξ as a function of the porosity in figure 12 for the first few hours of each experiment. For each concentration, all the data from these early times collapse extremely well onto the theoretical curve given by (6.12), which confirms that the system does indeed evolve without significant transport of solute initially. The predictions of (6.12) were made using a value of $T_b = -17\,^\circ$C, which is in the range $-20\,^\circ$C $< T_b < -16\,^\circ$C suggested by measurement.

The complete sets of porosity data are shown in figure 13. We observe a deviation from the similarity solution after about 2 hours for $c_0 = 0.1$ and about 4 hours for $c_0 = 0.2$. The porosity decreases in the lower part of the mushy layer and the deviation increases with time. We interpret this effect as a signature of convection inside the mush which leads to the formation of chimneys. Indeed when convection occurs, fresh liquid is driven into the mush which leads to more solidification of ice and a decrease of the horizontally averaged porosity even though there are channels free of ice.

7.3. *Onset of convection*

In their experiments, Wettlaufer *et al.* (1997) correlated the evolution of the mean porosity inside the mushy layer with the onset of convection. To deduce the mean (vertically averaged) solid fraction inside the mushy layer they used solute conservation to obtain

$$\overline{\phi}_E = \frac{\rho_e c_e V_e + (\rho_l c_l - \rho_0 c_0)V_0 + (\rho_m c_m - \rho_l c_l)h A_m}{\rho_m c_m \, h A_m}, \tag{7.1}$$
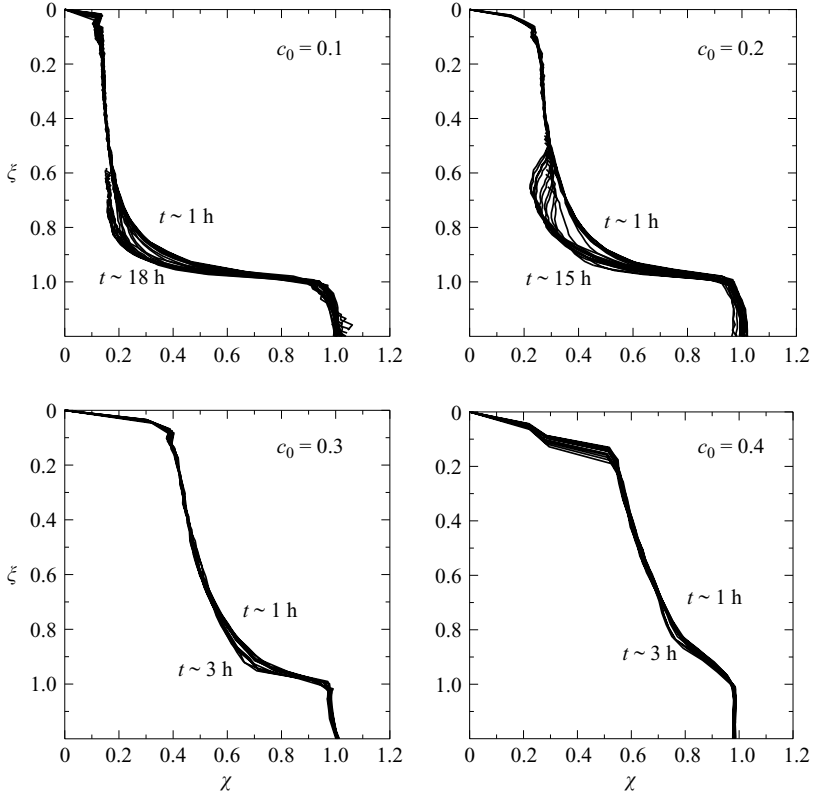
FIGURE 13. Similarity variable $\xi = z/h(t)$ as a function of porosity for the four experiments: $c_0 = 0.1$ (28 curves from 0.8 h to 17.9 h); $c_0 = 0.2$ (20 curves from 1.4 h to 15.1 h); $c_0 = 0.3$ (9 curves from 0.8 h to 2.7 h); $c_0 = 0.4$ (12 curves from 0.6 h to 3 h). The time increase is from right to left.

where V and A denote the volume and horizontal area of a region and the indices $e, l, m, s, 0$ designate the expansion tube, the liquid, mush, solid and initial liquid. We used equation (7.1) to determine the mean solid fraction in our laboratory experiments but we used our MRI data to calculate the mean solid fraction much more accurately by evaluating

$$\overline{\phi}_E = \int_0^1 \phi \, \mathrm{d}\xi,$$

using a cubic-spline interpolation of the porosity data.

The mean solid fraction as a function of the mush thickness is shown in figure 14(a) for the four MRI experiments. We can see that at early times the mean solid fraction is approximately constant with a value decreasing as the initial concentration increases. Using (6.12) we can deduce theoretically the mean porosity of the mush before convection begins:

$$\overline{\phi}_T \approx 1 - \int_0^1 \left(\frac{c_0}{c}\right)^{1/r} \mathrm{d}\xi. \tag{7.2}$$

In figure 14(b) the mean experimental solid fraction $\overline{\phi}_E$ at early times is shown as a function of the theoretical value $\overline{\phi}_T$ for the laboratory cubic and cylindrical
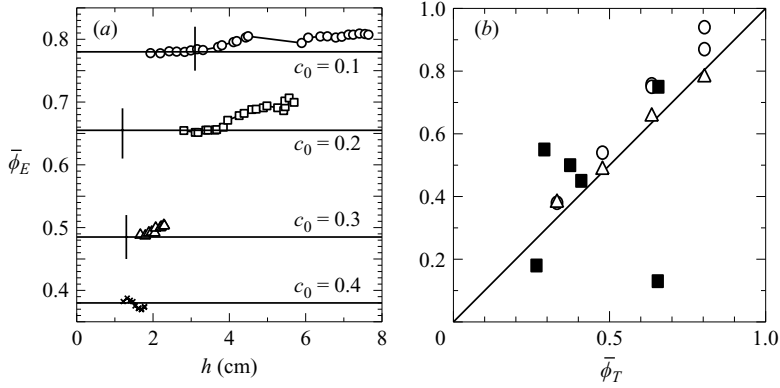
FIGURE 14. (*a*) Mean solid fraction across the mush as a function of the mush thickness for different solutions ($c_0 = 0.1, 0.2, 0.3$ and 0.4 from top to bottom). The horizontal lines represent the best constant fit for the solid fraction at early time (respectively 0.78, 0.685, 0.485 and 0.38) and the vertical lines represent the position of the top of the chimneys. (*b*) Experimental mean solid fraction at early times compared with the theoretical one (7.2) for the cubic (square), the cylindrical (circle) and the MRI (triangle) experiments.

tank experiments as well as for the MRI experiment. The straight line of unit slope indicates good agreement between theory and experiments, particularly for the MRI experiments.

Once a critical thickness is reached, we observe an increase of the solid fraction. The thickness at which this deviation occurs could indicate the onset of convection. The position of the top of the chimneys (i.e. the highest level to which chimneys extend) is also plotted in figure 14(*a*). We deduce, for example, that in the system with initial concentration $c_0 = 0.2$, convection began when the mushy layer was about 4 cm thick but is likely to have extended only to within 1 cm of the cooled plate. Therefore, the thickness of the convecting region, and the value of h relevant to the Rayleigh number (6.7) is only about 3 cm in this case.

There are two competing effects of the initial concentration. When the concentration is low, the permeability is low, so convection is retarded. When the concentration is high, the compositional difference across the mushy layer is small (for a given cold-plate temperature), so the driving density contrast is small and convection is again weak. The strongest effects of convection are seen at intermediate initial concentrations (here $c_0 = 0.2$).

7.4. *Bulk concentration*

An important property of solidified alloys is the local bulk concentration $\bar{c}(z)$ averaged over the microstructure. Variations in bulk concentration are called macrosegregation in the context of metallurgical castings, and determine the gross salinity and associated physical properties of sea ice, for example. During solidification, the bulk concentration is the local average concentration over the solid and liquid phases given by

$$\bar{c}(z) = \frac{\rho_l}{\bar{\rho}} \chi c = \left(1 + \frac{r\phi}{1 - \phi} \right)^{-1} c, \tag{7.3}$$

where c is the brine concentration inside the mush, depending only on the temperature via the liquidus relationship. The bulk concentration is plotted as a function of ξ in
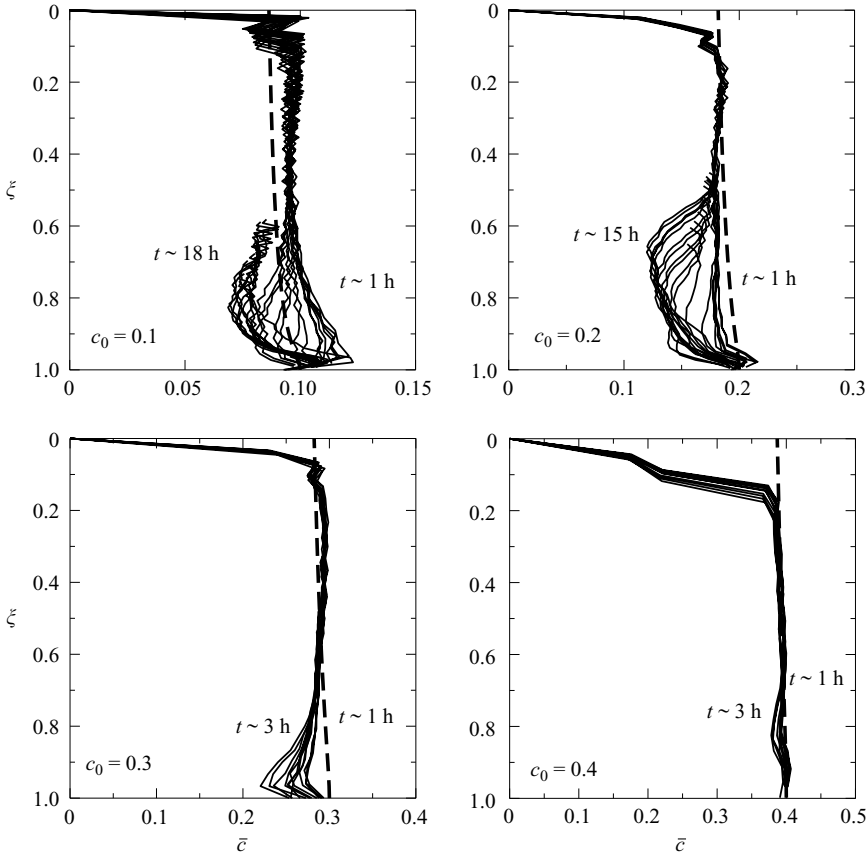
FIGURE 15. Similarity variable $\xi = z/h(t)$ versus bulk concentration $\bar{c}$ for the four experiments: $c_0 = 0.1$ (28 curves from 0.8 h to 17.9 h); $c_0 = 0.2$ (20 curves from 1.4 h to 15.1 h); $c_0 = 0.3$ (9 curves from 0.8 h to 2.7 h); $c_0 = 0.4$ (12 curves from 0.6 h to 3 h). The time increase is from right to left.

figure 15, using values of ϕ measured using MRI and the assumed linear temperature profile, for the four initial concentrations and the full range of experiments.

We clearly see that at early times the bulk concentration remains uniform and constant at the initial concentration and then, after a certain time depending on the initial concentration, we observe a deviation on the lower part of the curve towards lower concentrations. The total sucrose content of the mushy layer decreases in time, which shows that there is convective exchange between the mushy layer and the liquid region. The deviation seems restricted to the bottom part of the mushy layer, which is consistent with the MR images (figure 7), in which we see that the chimneys do not penetrate the whole mushy layer.

Indeed, if we subtract the first curve and plot this concentration difference as a function of the vertical position instead of the similarity variable we obtain the graphs plotted in figure 16. We observe that, except for their lower part close to the mush–liquid interface, all the curves appear to superimpose. This suggests that significant convection in this system is confined to the very lowest part of the mushy layer and that most of the chimney visualized in the final image of figure 8, for example, is in fact inactive. Initially, this is likely to be a consequence of the fact that the viscosity
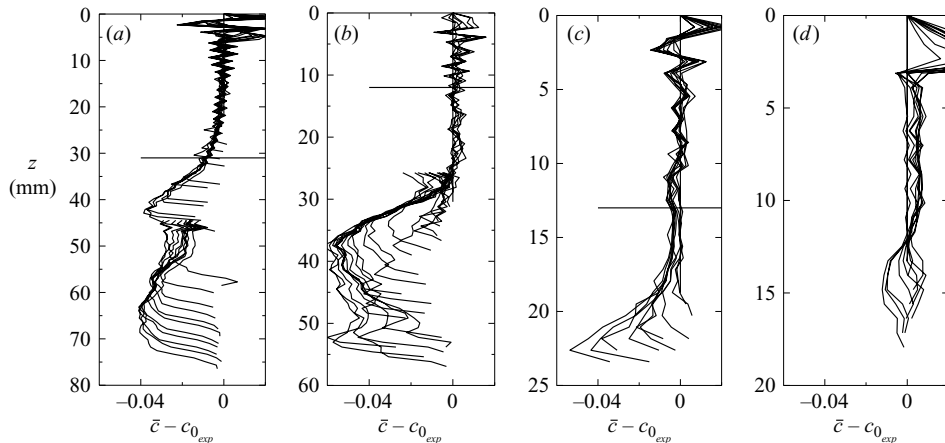
FIGURE 16. Difference between the local concentration ($\bar{c}(z)$ deduced using equation (7.3)) and the initial concentration as a function of the vertical position (z) for three of the four experiments: (a) $c_0 = 0.1$ (28 curves from 0.8 h to 17.9 h); (b) $c_0 = 0.2$ (20 curves from 1.4 h to 15.1 h); (c) $c_0 = 0.3$ (9 curves from 0.8 h to 2.7 h); (d) $c_0 = 0.4$ (11 curves from 0.7 h to 3.3 h). The time increase is from top to bottom. The horizontal lines correspond to the position of the top of the deeper chimneys.

is a strong function of composition. At later times it reflects the fact that convection causes the permeability to decrease, which causes the active zone to be close to the mush–liquid interface (e.g. Worster 1991).

Some preliminary confirmation of this comes from images of the vertical component of velocity, obtained using the MR velocity-imaging technique described at the end of §4. Examples are given in figure 17, which shows in a sequence of horizontal slices the porosity and the corresponding velocity images. Note that we are able to measure a velocity only close to the interface with the liquid and that even there not all chimneys are actively convecting. In those chimneys that are convecting, the maximum vertical velocity is about $200 \, \mu\mathrm{m \, s}^{-1}$.

Our measurements of bulk concentration can be used in another way to deduce the thickness of the actively convecting region of the mushy layer. Consider the temporal evolution of bulk composition in a fixed horizontal slice, at $z = h_0$ say. Figure 18(a) illustrates this for a slice located at $h_0 = 54$ mm from the cooling plate in the system with initial concentration $c_0 = 0.1$. We see that the bulk concentration at this position remains constant until time $t_1 \approx 5.5$ h, when the mush has a thickness h_1 say. Subsequently, the bulk concentration decreases until time $t_2 \approx 9.1$ h after which it again remains constant, at $\bar{c} = c_2$ say. Let $h_2 = h(t_2)$. Then we can deduce that the convecting zone had a thickness greater than $h_1 - h_0$ at the time t_1 that convection began to affect the horizontal slice at $z = h_0$, and had thickness $\Delta h = h_2 - h_0$ at time t_2. Note that if h_0 is greater than the thickness of the mushy layer at the time that convection began then $h_1 = h_0$. In this case, the constant bulk concentration before t_1 simply reflects the fact that the slice is in the liquid region, and the bulk concentration of the slice begins to decrease as soon as it is within the mushy layer.

Note from figure 18(b) that for times greater than t_2, the porosity is well represented by (6.12) using c_2 in place of c_0. On the other hand, it seems that the structure of the mushy layer continues to evolve at times greater than t_2. This is perhaps suggested by figure 18(c), which appears to show the area occupied by chimneys continuing to
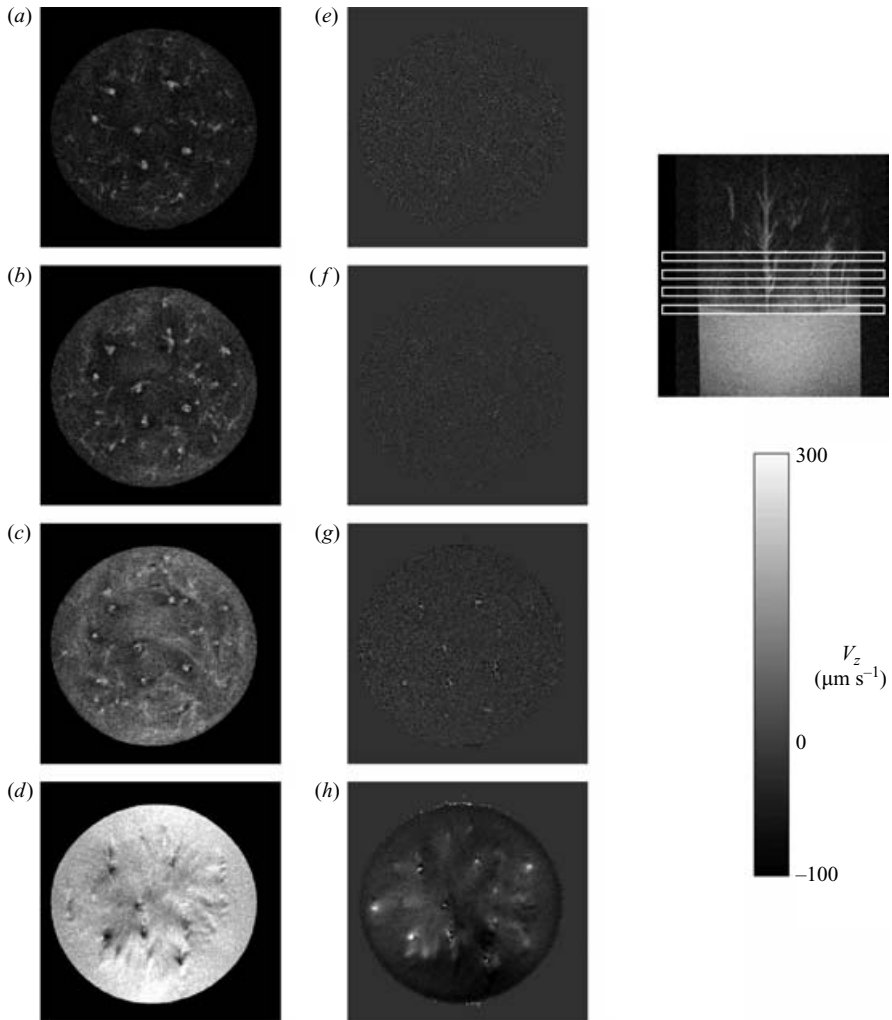
FIGURE 17. (*a–d*) Four intensity images identifying the position of the chimneys at different heights in the mushy layer (as shown in the side view on the right) and (*e–h*) corresponding velocity images at the same vertical position and time. The chimneys are seen to be active only close to the growing interface.

evolve, and the images below which show some qualitative evolution. This could be due to the fact that, as the mushy layer is growing, the local temperature is changing. On the other hand, it is possible that the convection continues and that the porosity data are not sensitive enough to show this evolution. The data available do not permit us to distinguish between these two hypotheses.

In figure 19, h_2 is plotted as a function of h_0 for the initial concentrations $c_0 = 0.1, 0.2$ and 0.3 and all the data can be fitted by a straight line corresponding to $h_2 \approx 1.23h_0$. Therefore it seems that the thickness of the actively convecting zone in this system is only about 23% of the total thickness of the mushy layer.

This confinement could be a consequence of the low permeability in the upper part of the mushy layer (Worster 1992) but is more likely to result from the strong dependence of the viscosity of the sucrose solutions on their temperature and
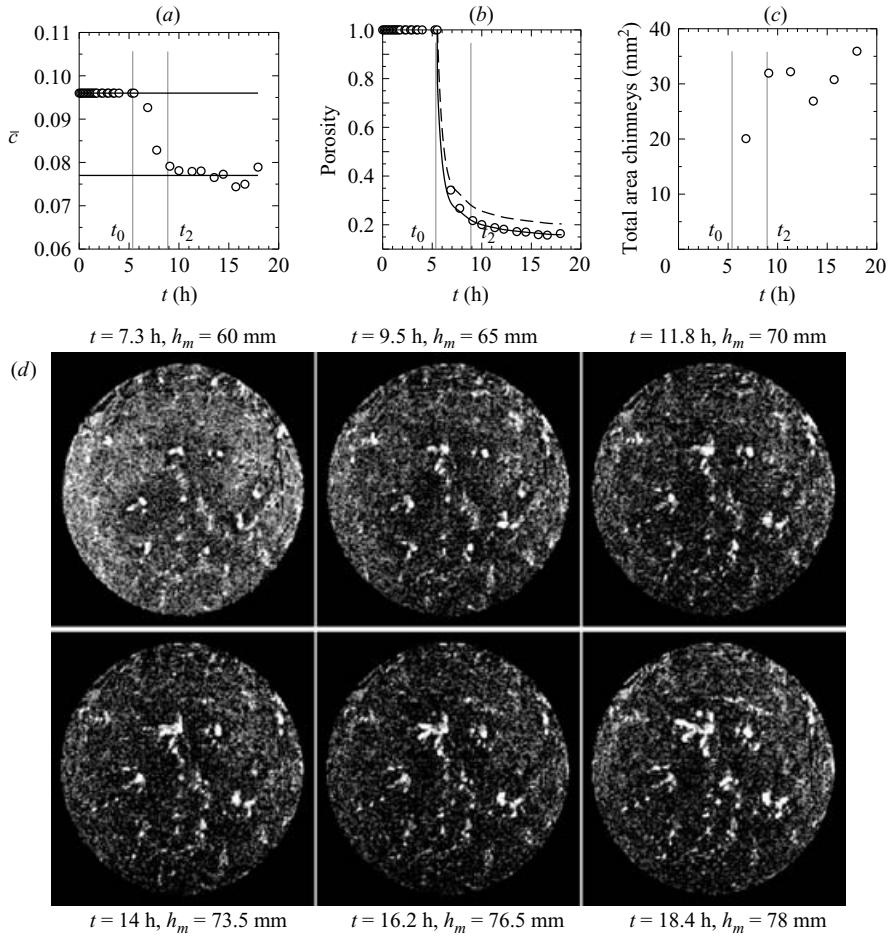
FIGURE 18. (*a*) Local concentration, (*b*) porosity and (*c*) area occupied by chimneys as functions of time for a horizontal slice located 54 mm away from the cooling plate with an initial concentration $c_0 = 0.1$, and (*d*) the corresponding medium-resolution images. The horizontal lines in (*a*) correspond to $c_0 \approx 0.108$ and $c_2 \approx 0.087$. The curves in (*b*) correspond to the solutions of (6.12) with c_0 (dashed) and c_2 (solid) as initial concentrations. The area occupied by chimneys (*c*) was deduced from the medium- and high-resolution images by subtracting the mean background and applying a threshold on pixel intensity to isolate 'liquid' regions. We counted as chimneys only those contiguous liquid regions with area in excess of $0.3\,\text{mm}^2$.

concentration resulting in a 'viscous stagnant lid' as studied by Davaille & Jaupart (1994) in the case of a pure liquid. Note, for example, that the convecting thickness seems to be rather insensitive to the porosity, which varies from around 0.2 to around 0.6 in our various experiments. On the other hand, the dynamic viscosity of the interstitial liquid varies from 1 to 10^4 mPa s from the bottom to the top of the mushy layer.

When convection occurs, the momentum equation is given by (6.6). If we suppose that convection begins when the driving density difference becomes comparable with the viscous dissipation, we obtain a condition for the onset of convection at a critical value of the porous Rayleigh number

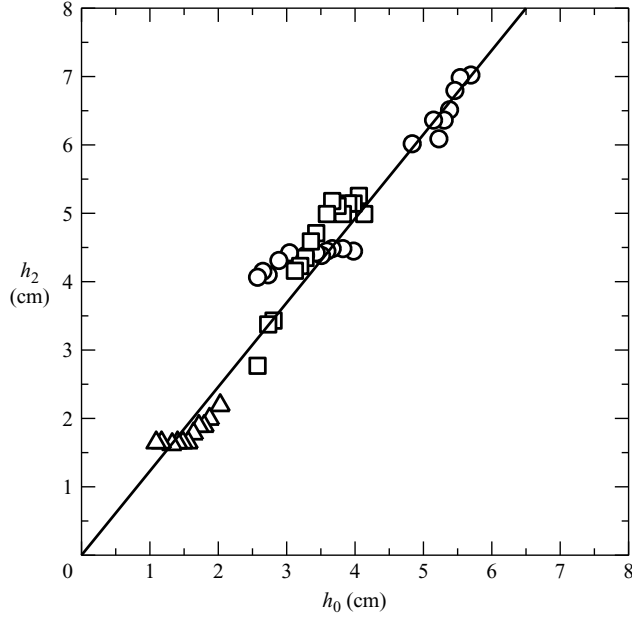$$Ra = \frac{\Delta \rho g \overline{\Pi} h}{\overline{\mu} \kappa}, \qquad (7.4)$$

FIGURE 19. Mush thickness h_2 when the convection stops as a function of h_0. The circles, squares and triangles correspond respectively to the initial concentrations $c_0 = 0.1, 0.2$ and 0.3. The straight line corresponds to $h_2 = 1.23 h_0$.

where $\overline{\mu}$ and $\overline{\Pi}$ are reference values for the viscosity and permeability (Worster 1992). The permeability (being a function of the solid fraction), the viscosity and the density difference are all functions of vertical position. To evaluate the influence of these variations we can calculate a Rayleigh number based on a supposed convecting zone of thickness $h\zeta$ at the base of the mushy layer, where $\zeta = 1 - \xi$ is a dimensionless thickness. In terms of ζ, the supposed linear temperature field is given by $T = T_\ell(c_0) - \Delta T \zeta$. A (minimum) local Rayleigh number for the convecting zones is then

$$Ra_\zeta = \frac{\alpha \Delta T \zeta \, g \, \Pi(\zeta) \, h\zeta}{\mu(\zeta) \kappa}, \tag{7.5}$$

where α is the constant of proportionality between density and temperature variations in a linear equation of state. Equation (2.5) is used to evaluate $\mu(\zeta)$, while the permeability is assumed to be given by

$$\Pi = d^2 \chi^3 / 12, \tag{7.6}$$

which is appropriate to a plate-like geometry, where d is the distance between the centres of the plates. With these assumptions, the leading-order variation of the local Rayleigh number is given by

$$Ra_\zeta \propto \zeta^2 \, e^{-\Delta T \zeta / T_\mu}, \tag{7.7}$$

which has a maximum at

$$\zeta_{max} = 2T_\mu / \Delta T. \tag{7.8}$$

Given that $T_\mu \approx 1.92\,°\text{C}$, from (2.5), and $\Delta T \approx 15\,°\text{C}$, (7.8) gives $\zeta_{max} \approx 0.25$. This is in good agreement with our experimental inference that the actively convecting zone was only about 23 % of the total mushy layer.
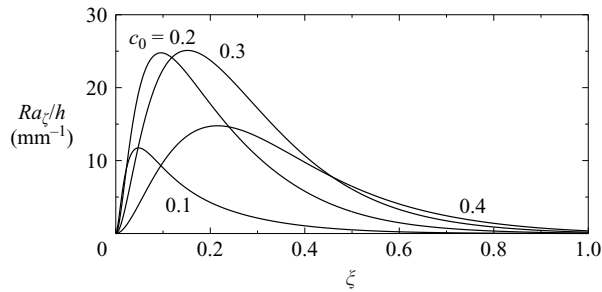
FIGURE 20. The Rayleigh number Ra_ζ characteristic of the actively convecting zone divided by the mush thickness h as a function of ζ for $T_b = -17\,^\circ\text{C}$ and three different initial concentrations.
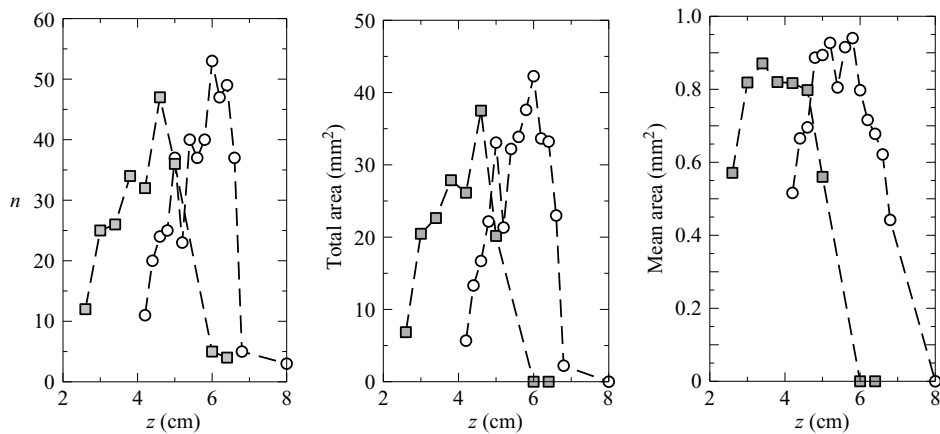

FIGURE 21. Evolution of the number of chimneys, total area of chimneys and mean area as a function of the position in the sample from the top plate after 11.3 h of solidification. The circles correspond to initial concentration $c_0 = 0.1$ and the squares to $c_0 = 0.2$. The thickness of the mushy layer was respectively 6 cm and 4 cm in the two cases.

We plot Ra_ζ/h as a function of ζ for $T_b = -17\,^\circ\text{C}$ and the three different initial concentrations in figure 20. The value of the maximum shows that the critical Rayleigh number in our case would be about 300, whereas Tait & Jaupart (1992) evaluate it to be around 25, but this value is highly dependent on the model chosen for the permeability.

7.5. *Evolution of the chimneys*

The evolution of the mushy layer can be additionally quantified by the evolution of its structure, for example the number of chimneys and their size. To make these measurements, we use the high-resolution images, and we process them as described in the caption to figure 18 to obtain the total area at a given position as a function of time. In figure 21 the evolution of the number of chimneys, the total area of chimneys and the mean area per chimney as a function of the position in the sample after 11.3 h of solidification is plotted for two initial concentrations $c_0 = 0.1$ and 0.2. Note that the thickness of the mushy layer was 6 cm and 4 cm respectively in the two cases. We see that, within the mushy layer, the number and the total area of chimneys increase with the vertical position, whereas the mean area is more or less constant with a mean

value of about $0.85\,\mathrm{mm}^2$ which corresponds to a typical diameter of about $1\,\mathrm{mm}$. The typical spacing between two chimneys was measured to be about $7\,\mathrm{mm}$.

8. Conclusions

Using MRI techniques, we have obtained images of the internal structure of a mushy layer during the solidification of ice from a sucrose solution. We are able to distinguish the ice platelet structure as well as observe the formation and evolution of the chimneys. The chimneys are branched and do not penetrate the whole mush in this system. Quantitative measurements of the local porosity distribution were made. The porosity data can be fitted by a similarity curve using a simple argument of local conservation of solute when there is no convection. Once convection starts, there is a deviation from this similarity solution toward a less-porous mushy layer, which can be explained by exchange of solute between the mushy layer and the liquid. The convection in our experiment seems to be limited to the lower part of the mushy layer and we have shown that a possible explanation is that the formation of a stagnant viscous region in the cold upper part of the layer causes convection to cease at a given vertical position as the mushy layer grows. Finally, we have shown that MRI is able to provide quantitative measurements of the liquid velocity inside the chimneys. These data provide us with new information about what is happening inside a mushy layer during solidification and in particular gives us information relating to convection inside the layer. The MRI technique opens up a new area of investigation in this subject. In future work we aim to develop this technique to obtain further quantitative data on the evolution of porosity during convection and the mass flux in chimneys and mush using more quantitative velocity images.

REFERENCES

BERGMAN, M. I., FEARN, D. R., BLOXHAM, J. & SHANNON, M. C. 1997 Convection and channel formation in solidifying Pb-Sn alloys. *Metall. Mater. Trans.* A **28A**, 859–866.

CALLAGHAN, P. T. 1991 *Principles of Nuclear Magnetic Resonance Microscopy*. Clarendon.

CALLAGHAN, P. T., DYKSTRA, R., ECCLES, C. D., HASKELL, T. G. & SEYMOUR, J. D. 1999 A nuclear magnetic resonance study of Antarctic sea ice brine diffusivity. *Cold Regions Sci. Tech.* **29**, 153–171.

CHEN, C. F. 1995 Experimental study of convection in a mushy layer during directional solidification. *J. Fluid Mech.* **293**, 81–98.

CHEN, C. F. & CHEN, F. 1991 Experimental study of directional solidification of aqueous ammonium chloride solution. *J. Fluid Mech.* **227**, 567–586.

CHIARELI, A. O. P. & WORSTER, M. G. 1992 On measurement and prediction of the solid fraction within mushy layers. *J. Cryst. Growth* **128**, 487–494.

COPLEY, S. M., GIAMEI, A. F., JOHNSON, S. M. & HORNBECKER, M. F. 1970 The origin of freckles in binary alloys. *IMA J. Appl. Maths* **35**, 159–174.

COTTIER, F., EICKEN, H. & WADHAMS, P. 1999 Linkages between salinity and brine channel distribution in young sea ice. *J. Geophys. Res.* **104**, 15859–15871.

DAVAILLE, A. & JAUPART, C. 1994 Transient high-Rayleigh-number thermal convection with large viscosity variation. *J. Fluid Mech.* **253**, 141–166.

EICKEN, H., BOCK, C., WITTIG, R., MILLER, H. & POERTNER, H.-O. 2000 Magnetic resonance imaging of sea-ice pore fluids: methods and thermal evolution of pore microstructure. *Cold Regions Sci. Tech.* **31**, 207–225.

FLEMINGS, M. C. & NEREO, G. E. 1967 Macrosegregation: Part I. *Trans. Metall. Soc. AIME* **239**, 1449–1461.

FUKUSHIMA, E. 1999 Nuclear magnetic resonance as a tool to study flow. *Annu. Rev. Fluid Mech.* **31**, 95–123.

GLADDEN, L. F., MANTLE, M. D. & SEDERMAN, A. J. 2005 Quantifying physics and chemistry at multiple length scales using magnetic resonance techniques. *Adv. Chem. Engng* **30**, chapter 2.

HUPPERT, H. E. & WORSTER, M. G. 1985 Dynamic solidification of a binary melt. *Nature* **314**, 703–707.

KERR, R. C., WOODS, A. W., WORSTER, M. G. & HUPPERT, H. E. 1989 Disequilibrium and macrosegregation during solidification of a binary melt. *Nature* **340**, 357–362.

KIMMICH, R. 1997 *NMR Tomography, Diffusometry, Relaxometry.* Springer.

KURZ, W. & FISHER, D. J. 1986 *Fundamentals of Solidification.* Trans. Tech. Publication.

MATHLOUTHI, M. & REISER, P. (Eds.) 1995 *SUCROSE Properties and Applications.* Blackie.

MANTLE, M. D. & SEDERMAN, A. J. 2003 Dynamic MRI in chemical process and reaction engineering. *Prog. Nucl. Magn. Reson. Spectr.* **43**, 3–60.

MENZEL, M. I., HAN, S. I., STAPF, S. & BLUMICH, B. 2000 NMR characterization of the pore structure and anisotropic self-diffusion in salt water ice. *J. Magn. Reson.* **143(2)**, 376–381.

NOTZ, D., WETTLAUFER, J. S. & WORSTER, M. G. 2005 A non-destructive method for measuring the salinity and solid fraction of growing sea ice in situ. *J. Glac.* **51**(172), 159–166.

RUDDICK, B. R. & SHIRTCLIFFE, T. G. L. 1979 Data for double diffusers : Physical properties of aqueous salt-sugar solutions. *Deep-Sea Res.* **26A**, 775–787.

SHIRTCLIFFE, T. G. L., HUPPERT, H. E. & WORSTER, M. G. 1991 Measurement of the solid fraction in the crystallization of a binary melt. *J. Cryst. Growth* **113**, 566–574.

TAIT, S., JAHRLING, K. & JAUPART, C. 1992 The planform of compositional convection and chimney formation in a mushy layer. *Nature* **359**, 406–408.

TAIT, S. & JAUPART, C. 1992 Compositional convection in a reactive crystalline mush and melt differentiation. *J. Geophys. Res.* **97**, 6735–6756.

TURNER, J. S. T., HUPPERT, H. E. & SPARKS, R. S. J. 1986 Komatiites 2. Experimental and theoretical investigations of post-emplacement cooling and crystallization *J. Petrol.* **27**(2), 397–437.

TURNER, J. S. T. & GUSTAFSON, L. B. 1981 Fluid motions and compositional gradients produced by crystallization or melting at vertical boundaries. *J. Volcanol. Geotherm. Res.* **11**, 93–125.

UNTERSTEINER, N. 1968 Natural desalination and equilibrium salinity profile of perennial sea ice. *J. Geophys. Res.* **73**, 1251–1257.

WETTLAUFER, J. S., WORSTER, M. G. & HUPPERT, H. E. 1997 Natural convection during solidification of an alloy from above with application to the evolution of sea ice. *J. Fluid Mech.* **344**, 291–316.

WORSTER, M. G. 1986 Solidification of an alloy from a cooled boundary. *J. Fluid Mech.* **167**, 481–501.

WORSTER, M. G. 1991 Natural convection in a mushy layer. *J. Fluid Mech.* **224**, 335–359.

WORSTER, M. G. 1992 Instabilities of the liquid and mushy regions during solidification of alloys *J. Fluid Mech.* **224**, 649–669.

WORSTER, M. G. 2000 Solidification of Fluids. In *Perspectives in Fluid Dynamics: a Collective Introduction to Current Research* (ed. G. K. Batchelor, H. K. Moffatt & M. G. Worster), pp. 393–446. Cambridge University Press.

WORSTER, M. G. 2002 Interfaces on all scales. In *Interfaces for the 21st Century* (ed. M. K. Smith, M. J. Miksis, G. P. Neitzel, G. B. McFadden & D. R. Cartwright). Imperial College Press.